Chemistry–A European Journal
Research Article
doi.org/10.1002/chem.202400858
Chemistry Europe
European Chemical Societies Publishing
www.chemeurj.org

Tripodal BODIPY-Tagged and Functional Molecular Probes: Synthesis, Computational Investigations and Explorations by Multiphoton Fluorescence Lifetime Imaging Microscopy

Marina Lledos,[a] David G. Calatayud,[b] Fernando Cortezon-Tamarit,[a] Haobo Ge,[a, c] Chararen Pourzand,[c, d] Stanley W. Botchway,[e] Mariona Sodupe,[f] Agustí Lledós,[f] Ian M. Eggleston,*[c, d] and Sofia I. Pascu*[a, d]

Dedicated to Professor Roger Alberto on his 65th birthday.

A range of novel BODIPY derivatives with a tripodal aromatic core was synthesized and characterized spectroscopically. These new fluorophores showed promising features as probes for *in vitro* assays in live cells and offer strategic routes for further functionalization towards hybrid nanomaterials. Incorporation of biotin tags facilitated proof-of-concept access to targeted bioconjugates as molecular probes. Computational explorations using DFT and TD-DFT calculations identified the most stable tripodal linker conformations and predicted their absorption and emission behavior. The uptake and speciation of these molecules in living prostate cancer cells was imaged by single- and two-photon excitation techniques coupled with two-photon fluorescence lifetime imaging (2P FLIM).

Introduction

Boron-dipyrromethene (BODIPY) derivatives have gained widespread popularity as imaging dyes for life sciences assays, owing to the vast range of advantages they offer, all rooted in a dipyrromethene system featuring a tetrasubstituted boron atom, typically in the form of a BF_2 unit. This is exemplified by commercial BODIPY dyes such as ER- and LysoTracker (Figure 1) which are currently widely used in organelle staining. Such derivatives have exceptional kinetic stability, substantial extinction coefficients, intense absorption, high quantum yields, and resilience in physiological environments[1–4] which has led to the development of a diverse array of BODIPY conjugates and corresponding bioconjugates as multifunctional cellular

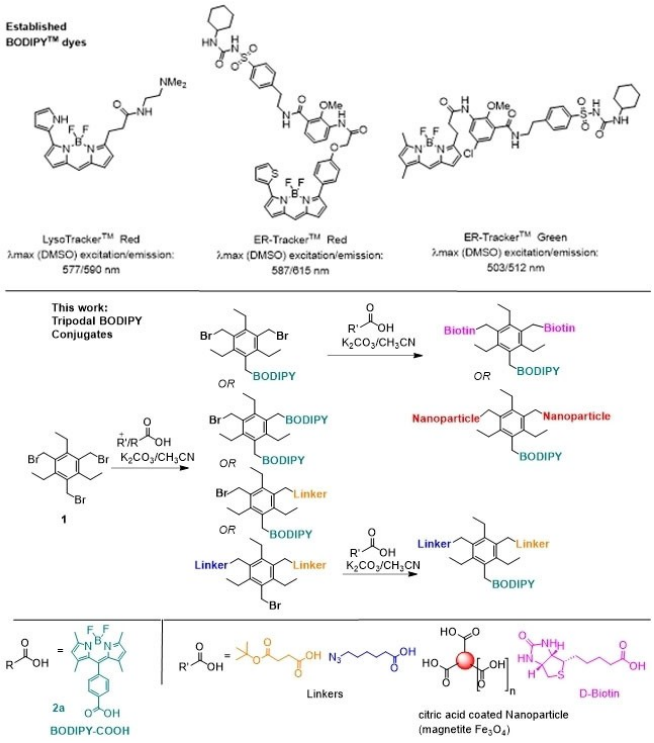

Figure 1. Overview of existing BODIPY-based imaging reagents, and novel architectures for tripodal BODIPY-tagged molecular probes (this work).

[a] Dr. M. Lledos, Dr. F. Cortezon-Tamarit, Dr. H. Ge, Prof. S. I. Pascu
Department of Chemistry, University of Bath
Bath, BA2 7AY (U.K.)
E-mail: S.Pascu@bath.ac.uk
ie203@bath.ac.uk
[b] Dr. D. G. Calatayud
Department of Inorganic Chemistry, Universidad Autonoma de Madrid, Francisco Tomas y Valiente 7, 28049, Madrid, Spain
[c] Dr. H. Ge, Dr. C. Pourzand, Dr. I. M. Eggleston
Department of Life Sciences, University of Bath, BA2 7AY, Bath, UK
[d] Dr. C. Pourzand, Dr. I. M. Eggleston, Prof. S. I. Pascu
Centre for Therapeutic Innovation, University of Bath, BA2 7AY, Bath, UK
[e] Prof. S. W. Botchway
STFC Research Complex at Harwell, Rutherford Appleton Laboratory, Harwell, Science and Innovation Campus, Harwell, Oxfordshire OX11 0QX, UK
[f] Prof. Dr. M. Sodupe, Prof. Dr. A. Lledós
Departament de Química, Universitat Autònoma de Barcelona
Cerdanyola del Vallès, 08193 Barcelona, Spain

Supporting information for this article is available on the WWW under https://doi.org/10.1002/chem.202400858

imaging probes. More recently, they have found application in multimodality imaging, seamlessly combining radioactivity and optical imaging. This versatility stems from the ability to label the fluorine unit within the BODIPY molecule with the radioisotope ^{18}F, facilitating multimodal imaging.[1–5]

To fully exploit the potential of BODIPY systems in multiplexing and multimodal imaging, there is a need for new approaches for the synthesis of BODIPY-containing scaffolds that may be effectively ligated with a range of targeting motifs or functional units. In this context, we report herein the design, synthesis and testing of new BODIPY-based molecular and nano-dimensional probes constructed around a tripodal scaffold with linking 'arms' (Figure 1) that can undergo further functionalization reactions to obtain potential multifunctional and targeted imaging probes using simple synthetic chemistry approaches and protocols.[6–11]

As proof-of-concept for bioconjugation strategies, we focused on the incorporation of a biotin tag. Chen *et al.* applied biotin conjugates to investigate the targeted delivery of anticancer drugs such as taxoids.[15] The internalization of such conjugates in cells, monitored by fluorescence imaging assays, indicated that cancer cells had higher affinity for the molecular probes, which was attributed to the overexpression of biotin receptors. In turn, this gave rise to a lower toxicity against normal cells. Biotin-tagged conjugates can be directed to cells via an induced mechanism involving avidin and streptavidin binding interactions. These are tetrameric proteins with extremely high affinities for biotin, and therefore can bind up to four molecules of biotin in a well-characterised fashion. This is commonly exploited for a range of applications, including immunological assays, flow cytometry, electron microscopy, nucleic acid hybridization and affinity chromatography;[16] all complementary to advancements in targeted therapies including pre-targeted methods with cell specific antibodies conjugated to streptavidin.[17] Moreover, biotin labelling of fluorophores has been successfully used in confocal fluorescence imaging of living cells,[18–20] by taking advantage of the increased prevalence of biotin receptors in cancer cells.

Iron oxide nanoparticles, in particular those composed of Fe_3O_4 (magnetite), can be used as contrast agents in magnetic resonance imaging (MRI) and are known to have superparamagnetic properties.[14,21–24] They are commonly used in a broad variety of therapeutic and diagnostic biomedical applications thanks to these properties that enable tracking of theranostic nanomedicines by MRI for *in vivo* applications to detect and characterize lesions, tumors, and to visualize body tissues. To expand the scope of hetero-topic molecular imaging probes the incorporation of a nanoparticulate iron oxide support with well-known biocompatibility and bioavailability into a BODIPY-based scaffold was explored along with the cellular uptake of the resulting nanohybrid denoted **Fe_3O_4-BODIPY**.

In the molecular architecture design deployed here, our focus was on the attachment of BODIPY to a tripodal scaffold (derived from **1**) which is known to adopt hindered and alternating up-down conformations for the $-CH_2-$ linking arms.[7a] As shown in Figure 1, this gave rise to a range of tripodal compounds and also facilitated the generation of multi-functional bioconjugate **5**, which contains two biotin tags and a BODIPY unit linked together in a tripodal framework (Figure 1). Multiphoton FLIM was then applied to directly explore whether conjugation impacts upon the characteristics of the BODIPY framework[25] and also to follow the presence of BODIPY-tagged compounds **2a**–**4a** and **5** inside cells after uptake. In this way the intracellular distributions could be explored by tracing compounds' individual lifetime distributions within cellular compartments.

Since biological samples absorb less strongly with increasing wavelength, excitation with red light and multiphoton imaging by near infra-red (NIR, here 810 nm) light may be used to reduce the magnitude of these problems. In earlier work, we showed that metal complexes of BODIPY can be used in time-resolved experiments that effectively reject scatter and short-lived fluorescence from the sample and that the nature of the chemical environment of BODIPY alters the lifetime response.[5] We have also already shown that it is possible to use 2P FLIM to monitor the cellular fate of kinetically stable 2P fluorescent nanomaterials as well as small molecules. Our previous work explored both time-gating methodologies (fluorescence lifetime microscopy, FLIM), and the application of novel probes for long wavelengths using 2P excitation.[20] This included the application of fluorescein-boronic acids, naphthylimide boronic acids and coumarin-boronic acids from the perspective of the interaction with cells in assays carried out at 810 nm, whilst carefully monitoring and minimising the effects of autofluorescence.[20] Time gating provided a method to observe a molecular species by a change in excited state, rather than by emission intensity; for example, we demonstrated in recent studies that a fluorescent free ligand has a significantly different lifetime compared to its bound form, and, depending on the systems involved, whether molecular or nanoparticulate in nature,[20] the bound-unbound components can show fluorescence lifetimes that differ significantly.

Results and Discussion

Synthesis and Characterization

The readily available precursor 1,3,5-*tris*(bromomethyl)-2,4,6-triethylbenzene **1** was chosen as a starting material to which a BODIPY label could be attached to then create potential new cellular imaging systems by orthogonal functionalization (see Scheme 1). The tripodal derivative **1** was synthesized following a previously described procedure.[6–7] Such scaffolds have been previously explored as the basis for a variety of molecular receptors featuring a range of thermodynamically stable conformations of such tripodal systems and interconversions thereof, and as precursors for photo-therapeutics.[7b]

BODIPY derivative **2a** incorporating a carboxylic acid function was synthesized,[5,8] and it was attached to the tripodal core **1** *via* a facile nucleophilic substitution reaction giving the key mono-substituted intermediate **3a** along with the corresponding di-substituted BODIPY scaffold **4a**. As shown in

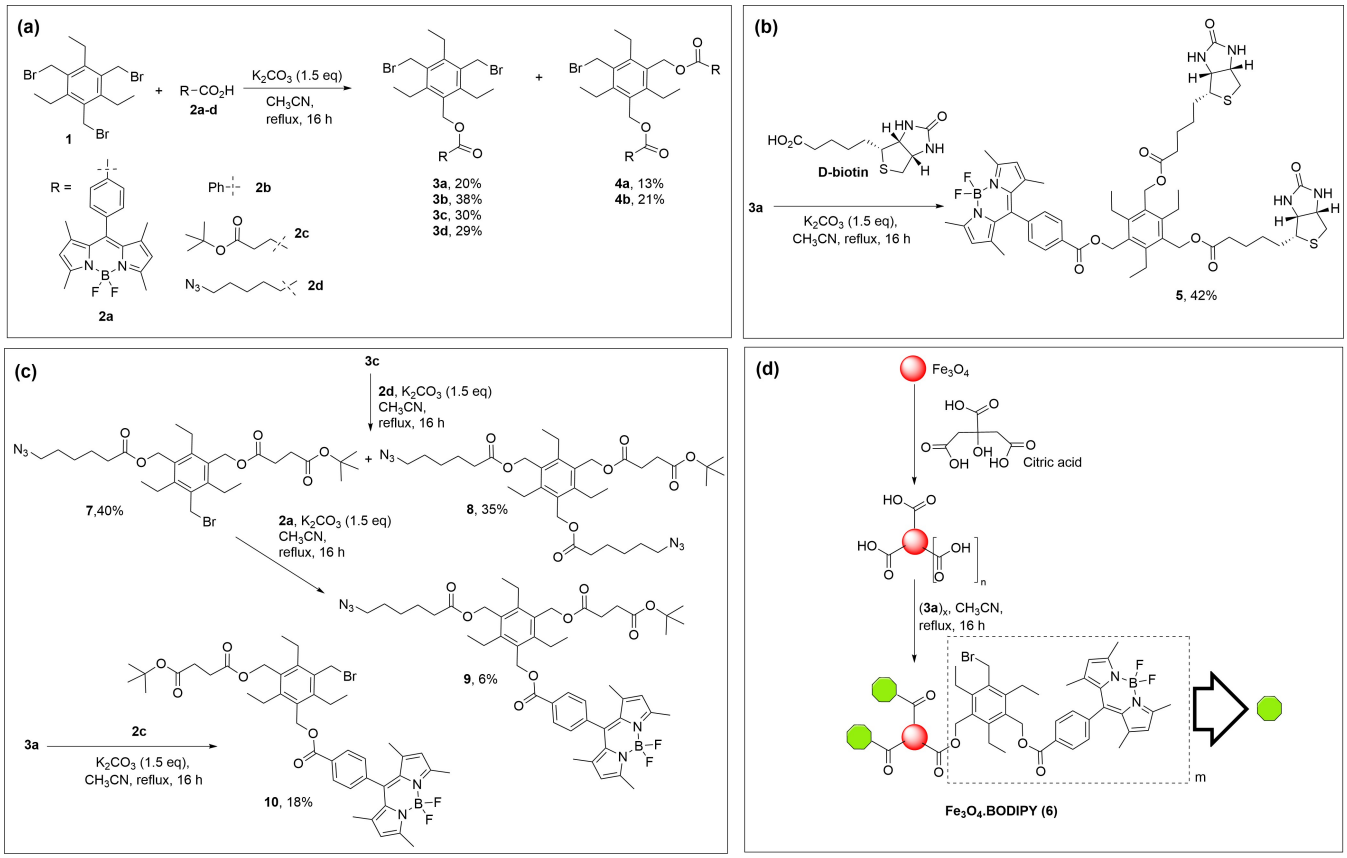

Scheme 1. (a) Synthesis of mono- and di-substituted scaffolds **3a**–**e** and **4a**–**b**. (b) Homo di-substution on BODIPY scaffold **3a** to produce targeted probe **5**. (c) Sequential substitutions on BOPIPY scaffold **3a** to generate orthogonal ligatable derivatives **9** and **10**. (d) Formation of Fe_3O_4-BODIPY nanoparticle mediated by the coating of Fe_3O_4 nanoparticles with citric acid and subsequent addition of a monofunctionalised BODIPY derivative **3a**.

Scheme 1(a), to probe the generality of this approach with respect to multi-functionalization and desymmetrization of the tripodal scaffold, displacements with other acids were also explored, including the bifunctional linkers **2c** and **2d** (see ESI). Using analogous methodology, **3a** was then converted to the biotin-targeted probe **5** (Scheme 1(b)). Sequential substitutions on **3c** gave rise to the hetero-tri-substituted BODIPY scaffold **9**, while conversion of **3a** to the BODIPY conjugate **10** led similarly to a tripodal compound featuring independent linker arms available for further orthogonal ligations. These compounds (**1**–**10**) were fully characterized spectroscopically as described in Figure 2 and in ESI (Figures S1–S31).

The excitation-emission characteristics were as expected for BODIPY-based dyes, close to the values typically found for established commercial dyes in this class (given in Figure 1, Top panel). The photophysical data for a selection of these new BODIPY probes is given in Figure 2, with their corresponding excitation-emission maxima discussed in the TDDFT calculation section below and detailed in ESI. Fluorescence quantum yields (QY) of **2a**, **3a**, **4a**, **5**, **9** and **10** were estimated at room temperature,[9,10] and the values in common organic solvents (DMSO, $CHCl_3$) were found to be closely comparable to that of the starting material (**2a**) (ESI, Tables S3-S4), and at *ca.* 0.1–0.5, collectively in line with the corresponding state-of-the-art in BODIPY derived compounds.[7]

To synthesise the nano-hybrid denoted **Fe_3O_4·BODIPY**, (Figure 3) the BODIPY derivative **3a** was used as outlined in Scheme 1(d). The precursor Fe_3O_4 nanoparticles were synthesized in the magnetite phase via a co-precipitation method.[27] Among all the different methods of synthesis of iron oxide nanoparticles, this was chosen due to its simplicity and ease in controlling the particle size.[28] Solutions of $FeCl_2$ and $FeCl_3$ were prepared using deoxygenated water and 2 M HCl(aq). They were mixed, and subsequently added dropwise with mechanical stirring to a basic solution of KOH. The formation of the black nanoparticles occurred instantly, and the nanoparticles were then collected by magnetic decantation and washed with water (see ESI). In this case, citric acid was used to coat, functionalise, and stabilise the magnetite particles. Citric acid was anchored onto the surface of freshly prepared nanoparticles by a direct addition method, with the carboxylic groups of this molecule rendering the nanoparticles more water-dispersible and providing sites for further functionalisation. Fe_3O_4 nanoparticles were dispersed in water and citric acid was added dropwise to the suspension until the pH reached 5. The dark brown mixture was mechanically stirred for 3 h at 85 °C, and after this time the resulting nanocomposite was isolated by centrifugation, and fully characterised in the solid state as well as in the dispersed phase (ESI, Figures S32–S34). Citric acid-coated Fe_3O_4 nanoparticles were dispersed in

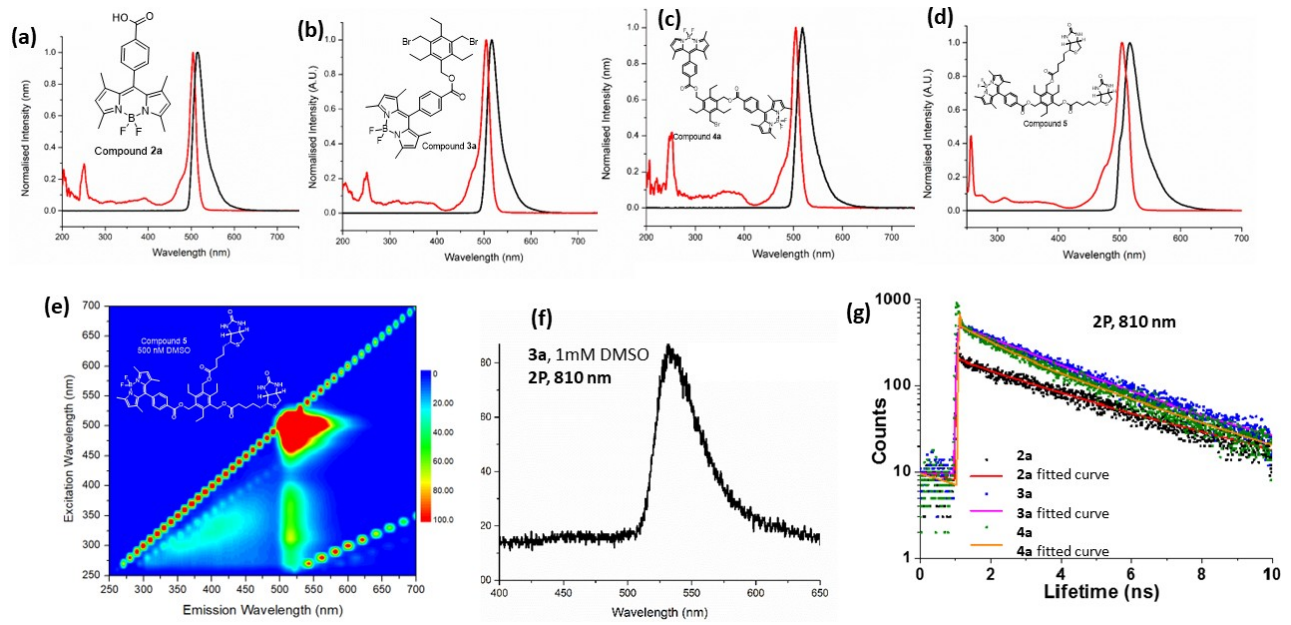

Figure 2. Excitation-emission data for BODIPY conjugates, 500 nM, $CHCl_3$ (a–d) and DMSO (e). 2P emission spectra of **3 a** (f). Comparison of 2P fluorescence lifetime decays (810 nm, 10 μM DMSO, TCSPC measurements).

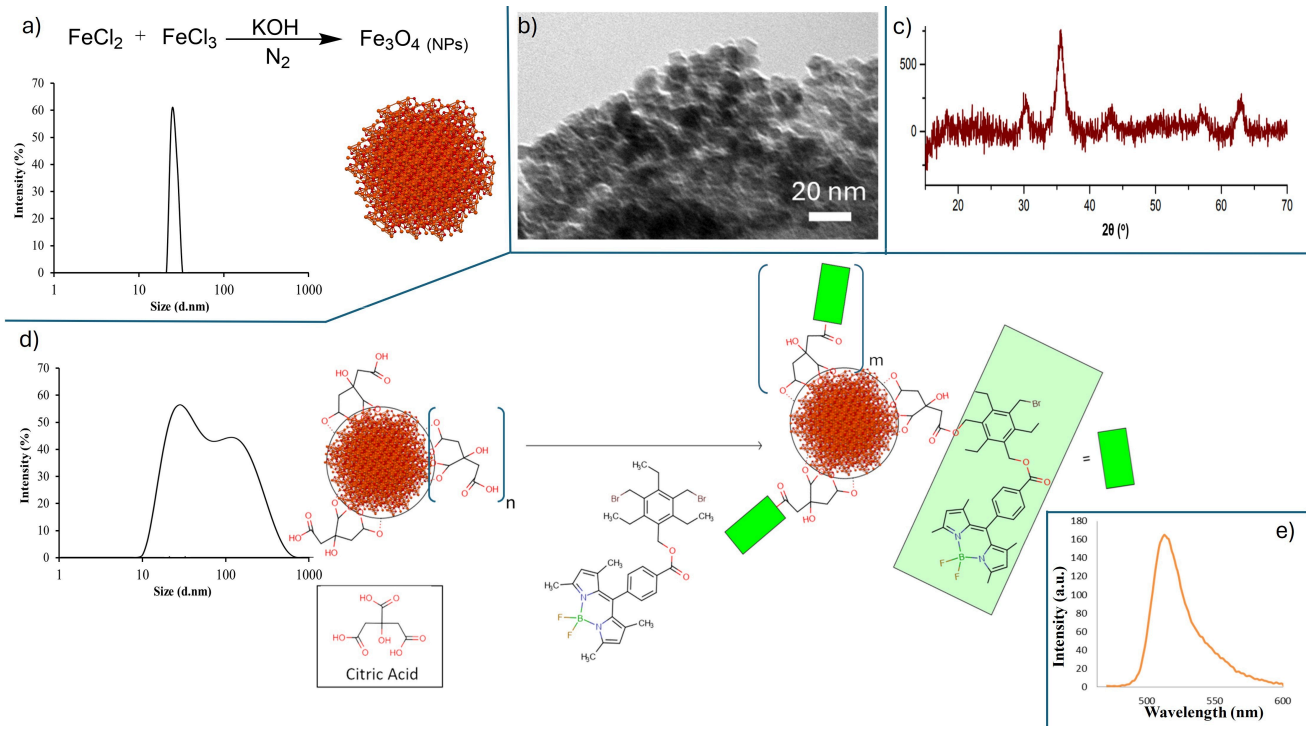

Figure 3. Overview of the formation of Fe_3O_4-BODIPY conjugate **6**, facilitated by the coating of magnetite Fe_3O_4 nanoparticles with citric acid and subsequent treatment with **3 a**. Selected characterisation details are TEM, XRD and DLS of Fe_3O_4 (a-c) and the effect of coating on the Fe_3O_4 seen by DLS (d). Fluorescence emission of Fe_3O_4-BODIPY nanoparticle in DMSO was recorded at 10 μg/mL for the redispersed particles (e). Extensive characterization details are given in ESI.

acetonitrile and subsequently treated with **3 a** by analogy with the previous experiments for the formation of derivatives **3 a**–**d** and **4 a**–**b** (see ESI) such that an ester bond was formed between the citric acid-coated nanoparticles and the tripodal core by nucleophilic substitution. The **Fe_3O_4BODIPY** nanocomposite (denoted species **6** in Scheme 1) was collected by centrifugation and washed with methanol and characterised by IR, UV and fluorescence spectroscopies, and these measurements are detailed in the ESI (Figures S32–S40, Tables S1–S2).

DFT Computational Prediction of Conformational Behavior

It has been shown that benzene-based tripodal systems such as **1** exhibit a high degree of conformational flexibility.[7] The conformational preferences of the core precursor **1**, the mono- and disubstituted BODIPY derivatives **3a** and **4a**, and biotin-tagged derivative **5** were investigated by DFT calculations with the M06 functionals in DMSO as solvent. The most stable conformations of all the compounds investigated are depicted in Figure 4, and the complete set of explored conformations can be found in the ESI. As expected, the preferred conformation of **1** is that with an alternating up-down disposition of the ethyl and bromomethyl substituents around the central aryl core. Rotating one $-CH_2Br$ arm to place one bromide up, on the same face as the ethyl groups, raises the energy by 1.6 kcal·mol^{-1} (ΔG in DMSO as solvent at the M06/6-311++G(2d,p) level). When one $-CH_2Br$ arm is substituted with a BODIPY derivative (**3a**), this preference is preserved, although the conformation with the BODIPY unit up, that is, on the same face as that of the ethyl groups, lies only 0.9 kcal·mol^{-1} above the most thermodynamically favourable conformer. When a second BODIPY unit is added to another $-CH_2Br$ arm (**4a**), the conformational preference is reversed. For this compound, the most stable conformer is that with one BODIPY substituent up and the other one down. The conformation with the two BODIPY units down (both on the opposite face with respect to the ethyl groups) is found to be 3.0 kcal·mol^{-1} above the most stable one. For **5** the conformation with both biotin groups on the same side of the aryl ring is 4.1 kcal·mol^{-1} more stable than that with them on opposite sides. Two N–H···O hydrogen bonds between ureido groups of both D-biotin groups confer higher stability to this conformation.

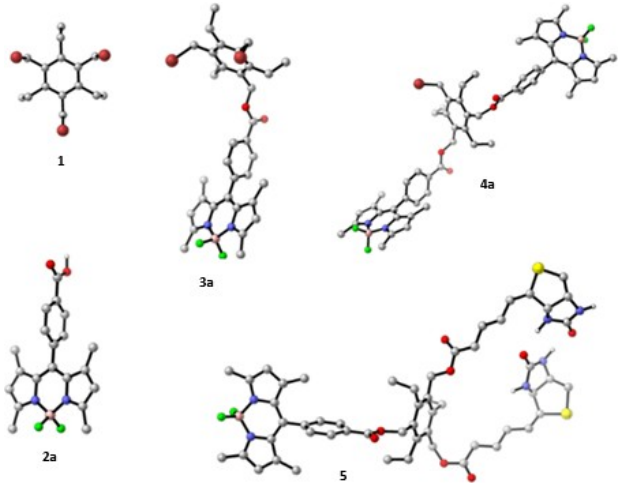

Figure 4. DFT-optimized geometries of the most stable conformers of tripodal scaffold **1**, BODIPY derivative **2a** and novel compounds **3a**, **4a**, and **5**.

The spectroscopic and photophysical characteristics of BODIPY dyes have been extensively studied by quantum mechanical calculations,[11] and their fluorescence mechanism rationalized by DFT and TDDFT calculations[12] BODIPYs are challenging systems for TDDFT calculations, which systematically overestimate the lowest singlet excitation energy,[29–32] giving differences with experimental wavelengths ranging from 60–100 nm.[33–35] Calibration calculations (see ESI) indicated that although similar results were obtained using different functionals and basis set, the M06/6-311++G(d,p) methodology give excitation energies closest to the experimental values, with differences lower than 60 nm (see details of calibration study in ESI). This is in line with the findings from a recently published theoretical study on isoindole-BODIPY derivatives.[23] Thus, linear response time-dependent DFT M06/6-311++G(d,p) calculations (LR-TDDFT) were performed to further analyze the electronic transitions responsible for the UV-visible spectra of the compounds in solution. The absorption spectra of the compounds in DMSO were computed with TDDFT calculations using the optimized ground state (S_0) geometries of the most stable conformations of these species. The results are summarized in Tables 1 and 2 and Figures 4–5.

Differences of around 60 nm between the experimental and computed λ_{abs} maxima can be observed. The maximum absorption peak in the UV-visible spectrum of BODIPY derivative **2a** results from a HOMO→LUMO transition and involves the π system of the BODIPY unit (Figure 5, left). This picture is not altered when the BODIPY derivative is anchored onto the tripodal core in **3a** (Figure 5, right). The same occurs in the disubstituted compound (**4a**), although in this case the presence of two BODIPY units places a S_2 state almost isoenergetic with the S_1 state. Neither the presence of two biotin units (**5**) changes this conclusion. Accordingly, the λ_{abs} maximum does not change in the four systems analyzed in line

Table 1. Selected parameters for the vertical excitation (UV-vis absorptions) of BODIPY derivatives **2a**, **3a**, **4a**, and **5** in DMSO. Calculated by TDDFT//M06/6-311++G(2d,p)//M06/6-31G(d,p), based on the optimized ground state geometries of the most stable conformations.

Compound	Electronic transition	Excitation energy (eV, nm)	f [a]	Composition [b]	Experiment λ_{abs} max (nm) 500 nM DMSO ($CHCl_3$)
2a	$S_0 \rightarrow S_1$	2.78, 446	0.632	H→L	503 (504)
3a	$S_0 \rightarrow S_1$	2.79, 445	0.604	H→L	505 (505)
4a	$S_0 \rightarrow S_1$ $S_0 \rightarrow S_2$	2.78, 446 2.79, 444	0.523 0.695	H→L H-1→L+1	504 (504)
5	$S_0 \rightarrow S_1$	2.79, 445	0.696	H→L	506 (505)

[a] Oscillator strength. [b] H stands for HOMO and L stands for LUMO

Table 2. Selected parameters for the emission spectra of BODIPY derivatives **2a**, **3a**, **4a**, and **5** in DMSO. Calculated by TDDFT at the M06/6-311++G(2d,p)//M06/6-31G(d,p) level of theory, based on the optimized S_1 state geometries of the most stable conformations.

Compound	Electronic transition	Excitation energy (eV, nm)	f [a]	Composition[b]	Experiment λ_{em} max (nm) 500 nM DMSO ($CHCl_3$)
2a	$S_1 \rightarrow S_0$	2.58, 481	0.539	H→L	516 (511)
3a	$S_1 \rightarrow S_0$	2.60, 476	0.539	H→L	515 (517)
4a	$S_1 \rightarrow S_0$ $S_2 \rightarrow S_0$	2.59, 479 2.78, 445	0.526 0.616	H→L H-1→L+1	515 (515)
5	$S_1 \rightarrow S_0$	2.58, 480	0.522	H→L	514 (516)

[a] Oscillator strength. [b] H stands for HOMO and L stands for LUMO.

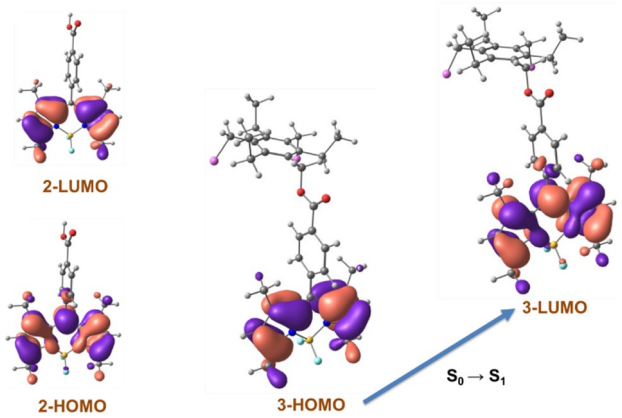

Figure 5. HOMO and LUMO orbitals of derivatives **2a** (left), and **3a** (right).

with the excitation and emission data observed experimentally (Tables 1 and 2 and ESI, Figures 41–S47, Tables S3-S4).

To investigate the TDDFT calculated emission spectra of the compounds, the geometry of the singlet excited state (S_1) was optimized for the most stable conformation of all of them, and the vertical excitation based on the S_1 geometry calculated. Optimized geometries of all the model compounds can be found in the ESI. The main structural changes in the excited state S_1 with respect to the ground state occur in the C–N and C–C distances of the central six-membered ring formed by the boron atom, the two N atoms and three C atoms of BODIPY. In **2a** the aromatic ring bearing the carboxylic acid function also rotates from a dihedral angle of 98.6° with respect to the BODIPY plane in S_0 to a value of 115.8° in S_1 and similar changes are found in model compounds **3**–**5** (see ESI, Tables S7-S11, Figures S77–S99). The TDDFT calculations indicate an emissive S_1 state for all the compounds. The calculated emissions differ in 30–40 nm from the experimentally observed emission bands (λ_{em} maxima). The emission spectra are more sensitive to BODIPY substitutions than the absorption ones, but they remain very close to the experimentally stablished ones.

In vitro Investigations by Single- and Two-photon Fluorescence Imaging

To evaluate the suitability of the new BODIPY-containing dyes **2a**, **3a**, **4a** and **5** as imaging agents *in vitro*, single-photon laser scanning confocal microscopy was carried out to study the uptake and distribution of these compounds in prostate cancer (PC-3) cells (Figure 6), given that simpler BODIPY systems are known to localize in the endoplasmic reticulum (ER).[2] The images obtained confirm the uptake of compounds **2a**, **3a** and **4a** by this type of cancer cell, with the majority of their emission lying within the green (~520 nm) and red channels (~620 nm). Furthermore, they do not seem to damage the cell morphology within the timescale of the imaging experiments (see ESI and Figures S49-S59).

Colocalization studies with ER-Tracker Red (λ_{ex} = 587 nm, λ_{em} = 615 nm), a known commercial dye which also features the BODIPY chromophore unit, were also carried out to understand the localization of these compounds throughout the cell cytoplasm and organelles, and a comparison with the multi-photon fluorescence lifetime microscopy (MP FLIM) investigations was carried out (ESI). When the ER-Tracker Red was used, emission in the red channel could be observed with 405, 488 and 561 nm wavelength lasers, as well as from the expected emission due to the fluorophores in the green and red channels (Figures 6, 7 and ESI, Figures S49–S56). Similarly, fluorescence intensity mode imaging using 2 photon excitation (810 nm) gave rise to very similar observations. (Figure 8, RHS micrographs, depicted in black-and-white). From these studies, it can be concluded that compounds **2a**, **3a**, **4a** and **5** all exhibit very strong fluorescence, and they distribute mainly in the cytoplasm, especially in the ER, as expected from BODIPY-tagged species, while there is no emission from the cellular nuclei (Figures 6–8). The cellular uptake of **Fe_3O_4-BODIPY** nanoparticle (synthesized and characterized as shown in ESI, and with confocal imaging shown in Figure 7A–C followed a similar pattern of behaviour where the cellular uptake is heavily influenced by the BODIPY tags (ESI, Figures S48, S57), albeit images revealed lower emission intensity as expected due to the quenching of the BODIPY emission caused by the presence of the super-paramagnetic Fe_3O_4 (magnetite) cores, and which was predicted by the low quantum yield of ca. 0.01, compared to the corresponding values for the molecular species investigated. [ESI, Tables S3–S4, Figure S48 and S57].

Research Article
doi.org/10.1002/chem.202400858
Chemistry Europe
European Chemical Societies Publishing

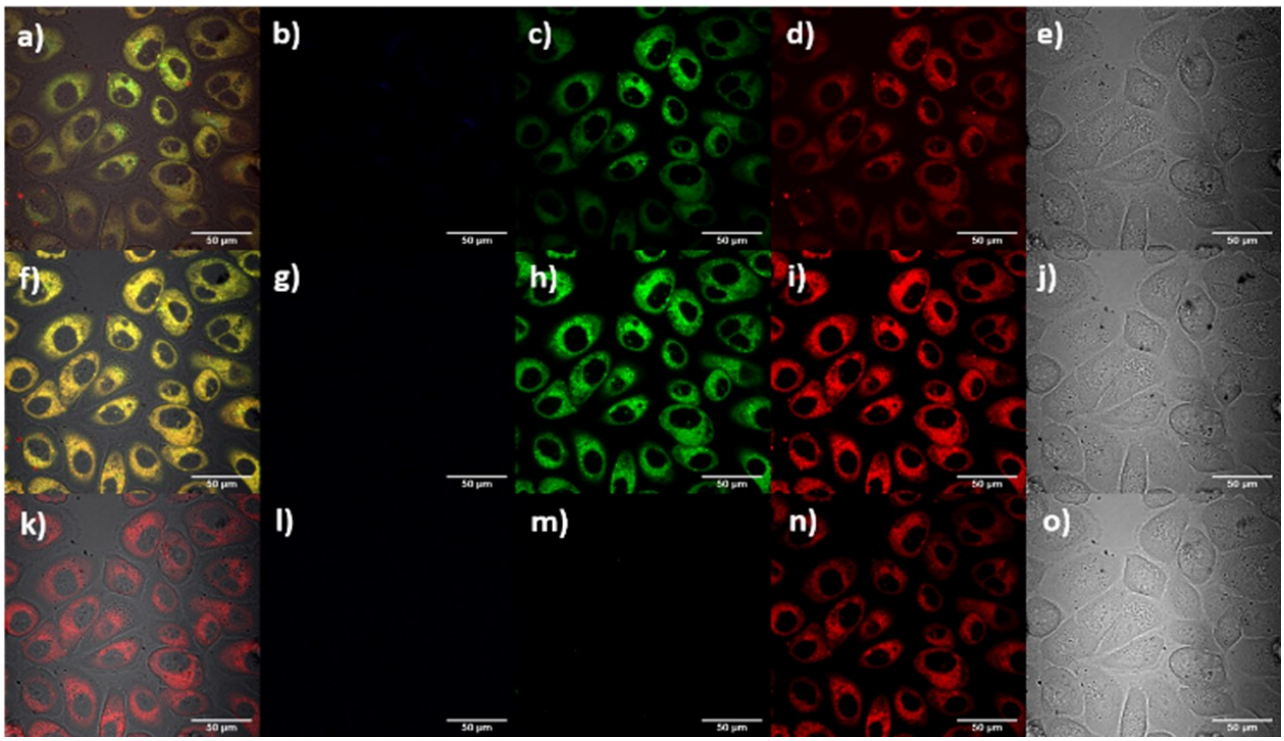

Figure 6. Single-photon laser scanning confocal microscopy of PC-3 cells incubated for 30 min at 37 °C with ER-Tracker Red, and 20 min with **3 a**, in colocalization assay. Final concentration: 10 μM in serum-free medium (1 % DMSO) solution of **3 a**, 1 μM ER-tracker™ Red. a–e) λ_{ex} = 405 nm; f–j) λ_{ex} = 488 nm; k-o) λ_{ex} = 561 nm. a, f, k) overlay of DIC-blue-green-red channels; b, g, l) blue channel (λ_{em} = 417–477 nm); c, h, m) green channel (λ_{em} = 500–550 nm); d, i, n) red channel (λ_{em} = 570–750 nm); e, j, o) DIC channel. Scale bar: 50 μm.

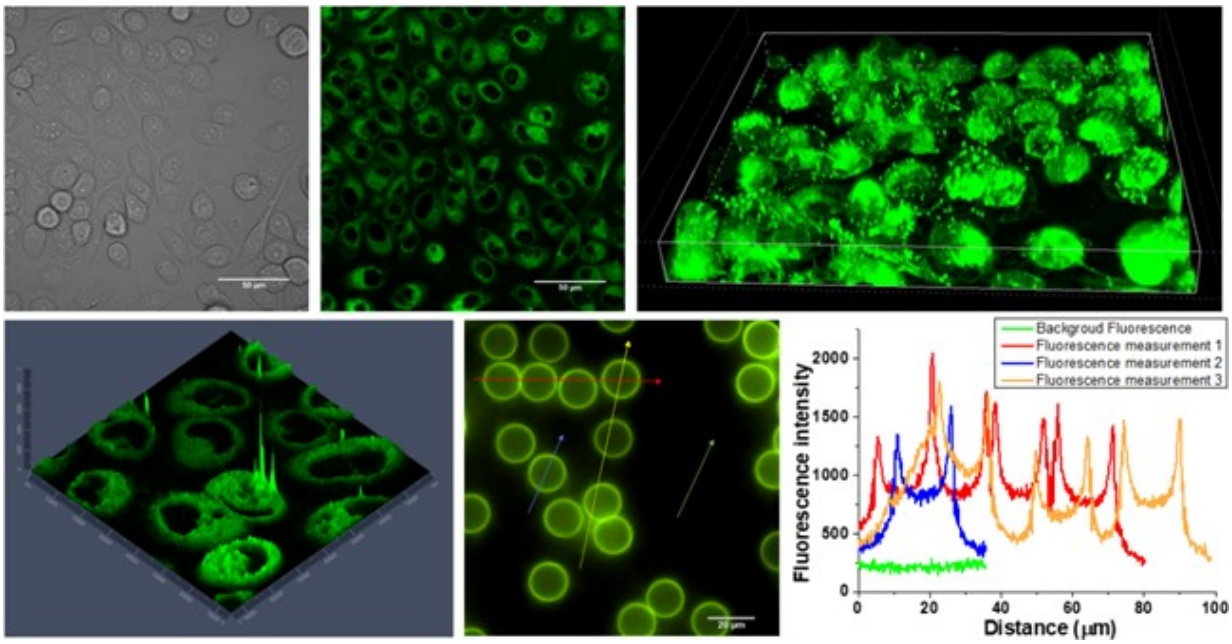

Figure 7. (A–C) Bright-field micrograph and corresponding laser scanning confocal microscopy imaging in 2D and 3D for the uptake of **Fe_3O_4.BODIPY** in PC-3 cells (scalebar 50 um). (D) Super resolution laser scanning confocal microscopy (Airyscan detection, 488 nm excitation) of 5 in PC-3 cells, 3D representation. Living PC-3 cells were incubated for 20 min. with either 10 μg/mL (1 : 99 DMSO:SFM) of **Fe_3O_4.BODIPY** dispersion or a 1 μM solution of **5** in 1 % DMSO. (E) Epifluorescence imaging of **5@avidin** polystyrene microbeads: excitation 460–500 nm; detection in green channel, λ_{em} = 500-550 nm. (F) Calibrated intensity showing relative fluorescence intensity of **5** taken across the field of view, which was compared to background (green line) and untreated beads (scalebar 20 μm).

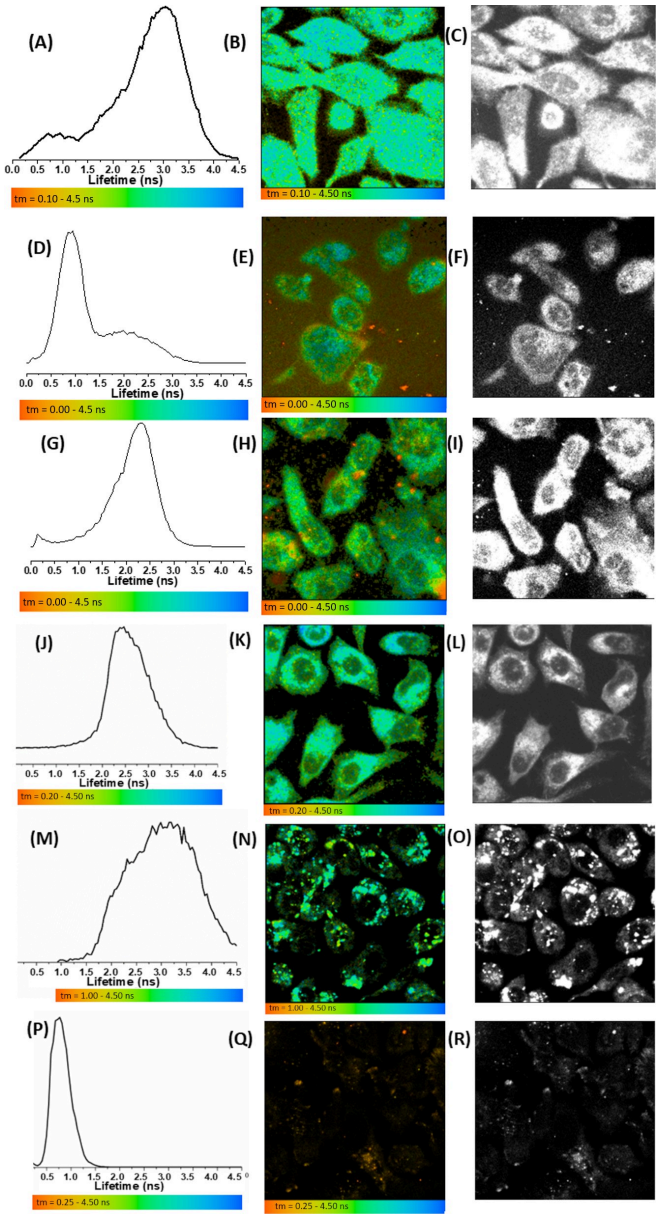

Figure 8. 2-Photon fluorescence lifetime in living PC-3 cells: Global distribution curves (A, D, G); fluorescence lifetime mapping of τ_m (B, E, H), and two-photon fluorescence intensity diagram of PC-3 cells treated with 10 μM solutions of each compound in SFM with 1% DMSO (C, F, I). λ_{ex} = 810 nm. Cells were incubated at 37 °C for 20 minutes with **2** (A–C), **3** (D–F), and **4** (G–I). Controls experiments include corresponding 2P FLIM data for known dye ER Tracker, 1 μM, 1% DMSO, (J–L) Lysotracker dye, 1 μM, 1% DMSO (M–O) and autofluorescence (1% DMSO) (P–R), all at 810 nm and 3 mW laser power. Additional controls including experiments using 910 nm 2P excitation are given in ESI (Figures S63–S73, and Table S5).

Table 3. Two-photon TCSPC data for compounds **2a**, **3a**, **4a** and **5**, 100 μM solutions in DMSO were excited at λex = 810 nm with a laser power between 0.5 and 1 mW. Lifetime decay data for **2a**, **3a**, **4a** and **5** were fitted on two components, τ_1 and τ_2 with % distribution a1 and a2 given below. For solutions in the 1–10 mM range in DMSO aggregation was observed which necessitated three exponential fitting for the lifetime parameters (ESI). Approximated value in ns is given in parentheses.

Compound	χ^2	τ_1 ps (ns)	a1 (%)	τ_2 ps (ns)	a2 (%)	τ_m ps (ns)
2a	1.10	1784 (1.78)	34.8	4366.3 (4.37)	65.2	3467 (3.47)
3a	1.02	2655 (2.65)	100	–	–	2655 (2.65)
4a	1.16	1133 (1.13)	43.2	3326 (3.33)	56.8	2379 (2.38)
5	0.89	1232 (1.23)	55.91	3219 (3.22)	44.09	2018 (2.02)

Fluorescence Lifetime Imaging Microscopy

Two-photon fluorescence lifetime imaging microscopy (MP-FLIM) using excitation at 810 as well as 910 nm was carried out with the new fluorescent compounds to study their lifetime characteristics both in solution (Table 3) and in living prostate cancer cells. Figure 8 shows the fluorescence lifetime maps for **2a**, **3a** and **4a in** PC-3 cells, and a model targeting approach using streptavidin-biotin interaction that characterises compound **5** is reported in Figure 9 D–F. Additional images are given in the ESI. The first experiments performed were to test the excited state lifetime of the new fluorophores in solution using DMSO as solvent. Time-correlated single-photon counting (TCSPC) was used for this purpose (ESI), followed by a FLIM *in vitro* uptake test using PC-3 cells. For these experiments, a two-photon microscopy setup was used, which was constructed around a Nikon TE2000-U inverted microscope with a modified Nikon EC2 confocal scanning system to enable near infra-red laser wavelength for FLIM investigations. A mode-locked titanium sapphire laser (Ti:Sapph, Mira; Coherent Lasers), was used to provide a laser light at a wavelength of 810 nm with 200 fs pulse width at 76 MHz.

To generate the 2-photon near infrared light (for 810 nm and 910 nm excitation), the Ti: Sapphire laser was pumped by a solid-state continuous wave 532 nm laser (Verdi V18; Coherent Laser). The samples were illuminated on the microscope stage, with a focused diffraction limited laser spot using a water-immersion objective (Nikon VC; numerical aperture of 1.2). Fluorescence emission was collected without a pinhole (non-descan mode), bypassing the confocal scanning system, and was passed through a BG39 (Comar) filter to block the near-infrared laser light. Line, frame, and pixel clock signals were

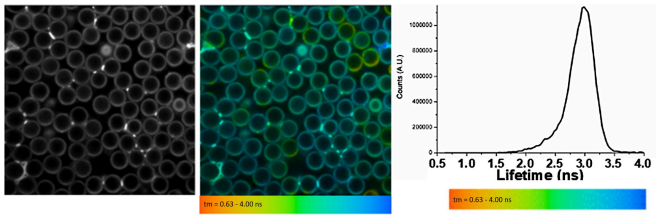

Figure 9. From left to right: Two-photon fluorescence intensity micrograph, fluorescence lifetime mapping and corresponding distribution of τ_m with rainbow-colored lifetime scale-bar (in ps) for streptavidin-coated microbeads, denoted **5@avidin**, λ_{ex} = 810 nm. Images were recorded for streptavidin microbeads after a 30-minute incubation with a 10 μM solution of 5 in 1:99 DMSO: SFM.

generated and synchronized with an external detector in the form of a fast hybrid photomultiplier tube (HPM100-40, Becker and Hickl, GmbH). The scanning system was linked to a time-correlated single-photon counting PC module SPC830 (Becker and Hickl) to generate the raw time-correlated single photon (TCSPC) decay at each pixel. Analysis of the pixel-by-pixel TCSPC data (using a SPCImage, V6 software) generated a FLIM image or map. Prior to FLIM data, the instrument was calibrated using samples with well-known lifetimes such as fluorescein, and results were compared with those ER Tracker and Lysotracker dyes (ESI, Figures S72–73).

Decay data were mostly fitted to a single exponential parameter as $f(t) = ae^{-t/\tau}$. A chi-square (χ^2) value is used to determine the goodness of fit, where values with a χ^2 between 0.9 and 1.2 were fitted on single exponential whilst values higher than this required close attention with consideration for the presence of other lifetime components.[36,37] In line with established protocols, the data includes for each measurement the goodness of fit of the decay curves given by χ^2, the lifetime of each component and their respective weighting if more then one component is present. The χ^2 value of 1.0 indicates an optimal single exponential fit, whilst χ^2 values of more than 1.3 indicates incomplete single exponential fit and such curves were subsequently fitted to more than one component. Life-times calculations (given in Tables 3 and 4) were obtained using SPCImage analysis software (Becker and Hickl, Germany) or Edinburgh Instruments F900 TCSPC analysis software.

In solution studies by the 2P excitation mode used hereby (using the TCSPC approach, Table 3) **3a** exhibited one component (exponential decay) for the fluorescence lifetime, while **2a**, **4a** and **5** have two-component contributions (τ_1, τ_2), and their occurrence can be due to interactions of the compound with the solvent (DMSO), or to the existence of isomers or pH-dependent protonated vs. non-protonated species in solutions and/or aggregation effects[13] (Table 3 and ESI, Table S5).

The 2P FLIM distribution and correlated intensities were obtained in PC-3 cells for **2a**, **3a** and **4a** (Figure 8 and Table 4) in side-by-side experiments. From the fluorescence lifetime distribution curves in PC-3 cells, the fluorescence lifetime distribution for **2a** is between 2.5 and 3.5 ns, approximately. For **3a**, the fluorescence lifetime distribution is between 0.5 and 1.5 ns, approximately, with a "tail" up to 3.0 ns but with a much lower number of counts.

Compound **4a** has a lifetime distribution between 1.6 and 2.8 ns, with a maximum number of counts at approximately 2.0 ns. The number of counts is high for all of the studied molecules, and for **2a** and **3a**, TCSPCs measured in several different spots in the cells showed that these compounds both have two different components for the lifetime distribution in cells, which can be seen in a major or minor proportion in the fluorescence lifetime distribution curves and are represented by the average global distribution curves with corresponding lifetime parameters in Table 4. All the data collected both in solution and in PC-3 cells is reliable with values for χ^2 falling within the 1.0–1.3 range.[14]

Table 4. 2P FLIM of **2a**, **3a**, **4a**, and **5** and standard dye controls in live PC-3 cells (10 μM dye, 1% DMSO, 37 °C at 810 nm excitation, 3–6 mW) and for **5** in streptavidin-coated microbeads (10 μM, 1% DMSO, 37 °C at 810 nm excitation, 5 mW). Control PC-3 exhibited weak autofluorescence under these conditions (1% DMSO, 37 °C at 810 nm excitation, 3–6 mW) was estimated 1.66 ± 0.44 ns.

Compound	Peak ± FWHM (ns)
2a	3.02 ± 0.63
3a	1.83 ± 0.90
4a	2.08 ± 0.45
5	2.92 ± 0.24
ER Red	2.44 ± 0.47
LysoRed	3.09 ± 0.84

Evaluation of 5 in Streptavidin-coated Microbeads

Compound **5**, which contains simultaneously BODIPY and two biotin groups, was incubated in PC-3 cells and these were imaged using single-photon laser scanning confocal microscopy as well as by super resolution confocal microscopy (Ayriscan detection mode). The green channel of the images recorded using the two different instruments show prostate cancer cells, whose morphology is not altered by the addition of the compound, and this localizes mainly in the cytoplasm (Figure 7D). Images in PC-3 cells were compared with those resulting from the uptake of particulate species **6** (**Fe_3O_4:BODIPY**), which showed aggregation (Figure 7A–C), and in microbeads treated with **5** (Figure 7E–F). *vide infra.* Commercial streptavidin-coated microbeads were used to show the attachment of the biotin-containing compound (**5**), and these were imaged using epifluorescence microscopy (Figure 7E) correlated with confocal and 2P-FLIM. The cancerous (hence the biotin-overexpressing) PC-3 cells and corresponding treated beads excited at 488 nm or 514 nm are strongly fluorescent and can be detected in the green channel of the confocal instruments (Airyscan detection) as well as by flow cytometry, using an adapted Alexa488 setup, and the binding analysis for the interaction of compound 5 with streptavidin-coated beads is given in Figure 10. Findings from flow cytometry correlate well with the epifluorescence spectroscopy calibrated intensity diagrams illustrating the relative fluorescence intensity profiles of the control and **5** across the field of view (Figure 7E and Figure 9). The fluorescence intensity profiles of streptavidin-coated beads, forming the assembly denoted as **5@avidin** are compared with the background intensity profile at sites of interest. Flow cytometry evaluation for the binding analysis of biotin-labeled compound **5** to **5@avidin** was carried out and compared to control experiments, confirming as expected the binding events detected under excitation at 488 nm. Similarly, the MP FLIM of streptavidin-coated microbeads confirmed the presence of **5** delineating these in the fluorescence lifetime as well as in intensity images as shown in Figure 9 and ESI (Figures S74–S75).

To evaluate the cytotoxicity of the new molecules in PC-3 cells, MTT (3-(4,5-dimethylthiazol-2-yl)-2,5-diphenyltetrazolium

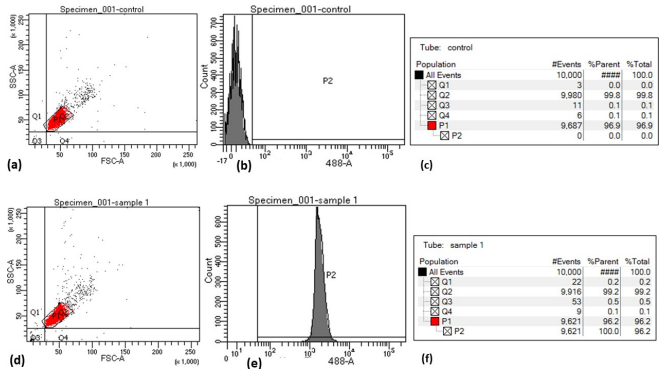

Figure 10. Flow cytometry binding analysis of the biotin-labelled compound 5 to streptavidin coated microbeads (denoted **5@avidin**). Scatter plots, histogram and tables show the flow cytometry of: (a–c) control, where P1 shows the region of measurement; (d–f). fluorescence emission intensity specific to AlexaFl488 type dyes with corresponding estimated binding events detected and counted in P1 region assignable to **5@biotin** (excitation 488 nm).

bromide) assays were carried out with the aim of estimating the IC_{50} value of the tripodal organic core used as starting material (**1**), the BODIPY carboxylic acid derivative (**2a**), and the tripodal systems with one and two of the bromomethyl arms substituted for a BODIPY derivative (**3a** and **4a**, respectively) in comparison with the biotin conjugate compound **5**. It can be observed from the

IC_{50} values (Table 5) that the cytotoxicity of the newly synthesized fluorophores (**3a** and **4a**) decreases significantly in comparison to that of the tripodal starting material (**1**). The biotinylating substitution of two bromomethyl arms as in **5** appears to have no significant effect on IC_{50} over the 48 h assays investigated (ESI, Table S6, Figure S76), and none of the compounds showed meaningful cytotoxicity within the timeline and concentration ranges of the cellular imaging experiments, *e.g.* up to1 h assays.

Conclusions

In summary, new potential imaging agents based on a symmetric tripodal molecule and incorporating one or two BODIPY units were synthesized, and their fluorescent properties investigated using single- and multiple-photon excitation sources. These correlated imaging approaches are unprecedented for tripodal BODIPY conjugates and open possibilities for new multiplexing assays. All new molecules easily translocated into PC-3 living cells, being retained in the cytoplasm without altering the cell morphology over the duration of imaging experiments (up to 2 h). Toxicity assays clearly showed a significant decrease in toxicity when substituting the arms of the starting material with a BODIPY derivative, making the materials more biocompatible. Colocalization studies showed the localization of the fluorophores within the endoplasmic reticulum. The fluorescence lifetime data show varying preexponential components amongst the different compounds and a close similarity to the multiphoton FLIM behavior of well-known ER dyes. The data revealed two or more components of exponential fitting functions for all the molecules tested. The possibility of bioconjugation for these compounds was demonstrated by adding biotin as a tag on a monofunctionalized tripodal molecule. Furthermore, a computational investigation of the new fluorophores showed that the absorption and emission properties of the new systems are not modified in comparison to the BODIPY starting material so that the tripodal core does not play a role in the electronic transitions of the molecule or hamper their usefulness as bioorthogonal and conjugatable new ER-tracking probes.

Table 5. Half-maximal inhibitory concentration IC_{50} in PC-3 cells after 48 h of treatment at 37 °C with **1**, **2a**, **3a**, **4a** and **5**. (The average data and corresponding standard deviation errors were collected from six repeated measurements).

Compound	IC_{50}/M
1	$(2.23 \pm 0.61) \cdot 10^{-6}$
2a	$(3.13 \pm 0.99) \cdot 10^{-4}$
3a	$(1.03 \pm 0.30) \cdot 10^{-4}$
4a	$(1.18 \pm 0.85) \cdot 10^{-4}$
5	$(2.42 \pm 0.19) \cdot 10^{-4}$

Data Statement

Supplementary Information available in ESI include: Synthetic protocols with full characterization details, spectroscopic and analysis data, nanoparticle characterization, cellular imaging and MTT assays. TD DTF data including cartesian coordinates for model compounds are also given in ESI. Data for this research are given in the Electronic supplementary (ESI) and available from the authors upon request.

Acknowledgements

The authors thank the ERC for funding through the Consolidator Grant O2Sense (617107), ERC PoC Tools-To-Sense (963937), and the University of Bath for the URSA-Science Strategic PhD studentship to ML. SIP also thanks the following grants for funding: STFC CDN + Biosensing and NIR Imaging of New Biomarkers for Prostate Cancer, BBSRC (BB/W019655/1: Multi User High- Content Confocal Fluorescence Microscope); EP/K0171 60/1: 'New manufacturable approaches to the deposition and patterning of graphene materials'; EP/L016354/1: EPSRC Centre for Doctoral Training in Sustainable Chemical Technologies EP/ G03768X/1: Doctoral Training Centre in Sustainable Chemical Technologies. DGC thanks to the Ministerio de Ciencia, Innovaci' on y Universidades (Spain) for funding (TED2021132779B-100 and TED2021-129876B–I00). The authors gratefully acknowledge the collaborative support from Megan Green and the Material and Chemical Characterisation Facility (MC2) at the University of Bath for technical support and assistance in this work.

Conflict of Interests

The authors declare no conflict of interest.

Data Availability Statement

The data that support the findings of this study are available in the supplementary material of this article.

Keywords: conjugatable tripodal D-biotin conjugates · multiplexing with BODIPY tags · Confocal microscopy and Airyscan super resolution · Multiphoton FLIM · TD-DFT calculations

[1] C. Bernhard, C. Goze, Y. Rousselin, F. Denat, *Chem. Commun.* **2010**, *46*, 8267.
[2] Y. Ni, J. Wu, *Org. Biomol. Chem.* **2014**, *12*, 3774.
[3] T. Kowada, H. Maeda, K. Kikuchi, *Chem. Soc. Rev.* **2015**, *44*, 4953–4972.
[4] A. Loudet, K. Burgess, *Chem. Rev.* **2007**, *107*, 4891–4932.
[5] P. A. Waghorn, M. W. Jones, M. B. M. Theobald, R. L. Arrowsmith, S. I. Pascu, S. W. Botchway, S. Faulkner, J. R. Dilworth, *Chem. Sci.* **2013**, *4*, 1430.
[6] K. J. Wallace, R. Hanes, E. Anslyn, J. Morey, K. V. Kilway, J. Siegel, *Synthesis (Stuttg).* **2005**, *2005*, 2080–2083.
[7] a) D. R. Turner, M. J. Paterson, J. W. Steed, *J. Org. Chem.* **2006**, *71*, 1598–1608; b) J. C. H. Chu, C. Yang, W.-P. Fong, C. T. T. Wong, D. K. P. Ng, *Chem. Commun.* **2020**, *56*, 11941–11944.
[8] A. Cui, X. Peng, J. Fan, X. Chen, Y. Wu, B. Guo, *J. Photochem. Photobiol. A* **2007**, *186*, 85–92.
[9] A. T. R. Williams, S. A. Winfield, J. N. Miller, *Analyst* **1983**, *108*, 1067.
[10] A. M. Brouwer, *Pure Appl. Chem.* **2011**, *83*, 2213–2228.
[11] a) R. Ziessel, G. Ulrich, A. Harriman, *New J. Chem.* **2007**, *31*, 496; b) B. Shen, K. H. Jung, S. Ye, C. A. Hoelzel, C. H. Wolstenholme, H. Huang, Y. Liu, X. Zhang, *Aggregate* **2022**, *2023*; 4:e301. DOI 10.1002/agt2.301.
[12] H. P. Kalofonos, M. Rusckowski, D. A. Siebecker, G. B. Sivolapenko, D. Snook, J. P. Lavender, A. A. Epenetos, D. J. Hnatowich, *J. Nucl. Med.* **1990**, *31*, 1791–6.
[13] C. E. Chivers, A. L. Koner, E. D. Lowe, M. Howarth, *Biochem. J.* **2011**, *435*, 55–63.
[14] Y.-P. Wu, C. Y. Chew, T.-N. Li, T.-H. Chung, E.-H. Chang, C. H. Lam, K.-T. Tan, *Chem. Sci.* **2018**, *9*, 770–776.
[15] S. Chen, X. Zhao, J. Chen, J. Chen, L. Kuznetsova, S. S. Wong, I. Ojima, *Bioconjugate Chem.* **2010**, *21*, 979–987.
[16] E. P. Diamandis, T. K. Christopoulos, *Clin. Chem.* **1991**, *37*, 625–36.
[17] H. P. Lesch, M. U. Kaikkonen, J. T. Pikkarainen, S. Ylä-Herttuala, *Expert Opin. Drug Delivery* **2010**, *7*, 551–564.
[18] F. D'Hooge, S. A. Elfeky, S. E. Flower, S. I. Pascu, A. T. A. Jenkins, J. M. H. van den Elsen, T. D. James, J. S. Fossey, *RSC Adv.* **2012**, *2*, 3274.
[19] Q. Sun, J. Qian, H. Tian, L. Duan, W. Zhang, *Chem. Commun.* **2014**, *50*, 8518.
[20] a) H. Ge, P. J. Riss, V. Mirabello, D. G. Calatayud, S. E. Flower, R. L. Arrowsmith, T. D. Fryer, Y. Hong, S. Sawiak, R. M. J. Jacobs, S. W. Botchway, R. M. Tyrrell, T. D. James, J. S. Fossey, J. R. Dilworth, F. I. Aigbirhio, S. I. Pascu, *Chem* **2017**, *3*, 437–460; b) M. Green, H. Ge, S. W. Botchway, T. D. James, S. I. Pascu, *RSC Chemical Biology* **2023**, *4*(12), 1082–1095; c) H. Ge, F. Cortezon-Tamarit, H. C. Wang, A. C. Sedgwick, R. L. Arrowsmith, V. Mirabello, S. W. Botchway, T. D. James, S. I. Pascu, *Nanoscale* **2019**, *11*(19), 9498; d) M. Lledos, V. Mirabello, S. Sarpaki, H. Ge, H. J. Smugowski, L. Carroll, E. O. Aboagye, F. I. Aigbirhio, S. W. Botchway, J. R. Dilworth, D. Gonzalez Calatayud, P. Plucinski, G. Price, S. I. Pascu, *ChemNanoMat* **2018**, *4*(4), 361.
[21] K. T. Komoto, T. Kowalczyk, *J. Phys. Chem. A* **2016**, *120*, 8160–8168.
[22] E. A. Briggs, N. A. Besley, D. Robinson, *J. Phys. Chem. A* **2013**, *117*, 2644–2650.
[23] M. E. Alberto, B. C. De Simone, G. Mazzone, A. D. Quartarolo, N. Russo, *J. Chem. Theory Comput.* **2014**, *10*, 4006–4013.
[24] a) L. Jiao, C. Yu, J. Wang, E. A. Briggs, N. A. Besley, D. Robinson, M. J. Ruedas-Rama, A. Orte, L. Crovetto, E. M. Talavera, J. M. Alvarez-Pez, M. Van der Auweraer, N. Boens, *RSC Adv.* **2015**, *5*, 89375–89388; b) E. Cheraghipour, S. Javadpour, A. R. Mehdizadeh, *J. Biomed. Sci. Eng* **2012**, *5*, 715–719.
[25] J. Shao, H. Sun, H. Guo, S. Ji, J. Zhao, W. Wu, X. Yuan, C. Zhang, T. D. James, *Chem. Sci.* **2012**, *3*, 1049–1061.
[26] X. Zhou, W. Xu, Y. Wang, Q. Kuang, Y. Shi, L. Zhong, Q. Zhang, *J. Phys. Chem. C* **2010**, *114*, 19607–19613.
[27] A. P. Philipse, M. P. B. van Bruggen, C. Pathmamanoharan, *Langmuir* **1994**, *10*, 92–99.
[28] A. Sood, V. Arora, J. Shah, R. K. Kotnala, T. K. Jain, *Mater. Sci. Eng. C* **2017**, *80*, 274–281.
[29] B. Mao, D. G. Calatayud, V. Mirabello, N. Kuganathan, H. Ge, R. M. J. Jacobs, A. M. Shepherd, J. A. Ribeiro Martins, J. Bernardino De La Serna, B. J. Hodges, S. W. Botchway, S. I. Pascu, *Chem. A Eur. J.* **2017**, *23*, 9772–9789.
[30] S. Chibani, A. D. Laurent, B. Le Guennic, D. Jacquemin, *J. Chem. Theory Comput.* **2014**, *10*, 4574–4582.
[31] M. R. Momeni, A. Brown, *J. Chem. Theory Comput.* **2015**, *11*, 2619–2632.
[32] D. Jacquemin, Y. Zhao, R. Valero, C. Adamo, I. Ciofini, D. G. Truhlar, *J. Chem. Theory Comput.* **2012**, *8*, 1255–1259.
[33] J. A. Tyson, V. Mirabello, D. G. Calatayud, H. Ge, G. Kociok-Köhn, S. W. Botchway, G. Dan Pantoş, S. I. Pascu, *Adv. Funct. Mater.* **2016**, *26*, 5641–5657.
[34] A. Schlachter, A. Fleury, K. Tanner, A. Soldera, B. Habermeyer, R. Guilard, P. D. Harvey, *Molecules* **2021**, *26*, 1780.
[35] Q. Alkhatib, W. Helal, A. Marashdeh, *RSC Adv.* **2022**, *12*, 1704–1717.
[36] A. Ahmed, J. Schoberer, E. Cook, S. W. Botchway, *Methods Mol. Biol.* **2021**, 287–301.
[37] S. W. Botchway, K. M. Scherer, S. Hook, C. D. Stubbs, E. Weston, R. H. Bisby, A. Parker, *J. Microsc.* **2015**, *258*, 68–78.

Manuscript received: February 29, 2024
Accepted manuscript online: June 18, 2024
Version of record online: August 12, 2024